Journal of The Electrochemical Society, **152** (11) A2159-A2169 (2005)
0013-4651/2005/152(11)/A2159/11/$7.00 © The Electrochemical Society, Inc.

Correlation of Water Activation, Surface Properties, and Oxygen Reduction Reactivity of Supported Pt–M/C Bimetallic Electrocatalysts Using XAS

Maggie Teliska,[a,c,*] Vivek S. Murthi,[b,d] Sanjeev Mukerjee,[b,*] and David E. Ramaker[a,*,z]

[a]*Department of Chemistry, George Washington University, Washington, DC 20052, USA*
[b]*Department of Chemistry, Northeastern University, Boston, Massachusetts 02115, USA*

An analysis of X-ray absorption spectroscopy (XAS) data [X-ray absorption near-edge structure (XANES) and extended X-ray absorption fine structure (EXAFS)] at the Pt L_3 edge for Pt–M bimetallic materials (M = Co, Cr, Ni, Fe) and at the Co K edge for Pt–Co is reported for Pt–M/C electrodes in $HClO_4$ at different potentials. The XANES data are analyzed using the $\Delta\mu$ method, which utilizes the spectrum at some potential V minus that at 0.54 V reversible hydrogen electrode (RHE) representing a reference spectrum. These $\Delta\mu$ data provide direct spectroscopic evidence for the inhibition of OH chemisorption on the cluster surface in the Pt–M. This OH chemisorption, decreasing in the direction Pt > Pt–Ni > Pt–Co > Pt–Fe > Pt–Cr, is directly correlated with the previously reported fuel cell performance (electrocatalytic activities) of these bimetallics, confirming the role of OH poisoning of Pt sites in fuel cells. EXAFS analysis shows that the prepared clusters studied have different morphologies, the Pt–Ni and Pt–Co clusters were more homogeneous with M atoms at the surface, while the Pt–Fe and Pt–Cr clusters had a "Pt skin." The cluster morphology determines which previously proposed OH inhibition mechanism dominates, the electronic mechanism in the presence of the Pt skin, or lateral interactions when M-OH groups exist on the surface.
 [DOI: 10.1149/1.2040949]

Manuscript submitted April 8, 2005; revised manuscript received June 15, 2005. Available electronically September 30, 2005.

Platinum-based bimetallics for use as cathodes in PEMFCs (polymer electrolyte membrane fuel cells) have gained considerable attention in recent years, in part because bimetallic catalysts offer a cost effective alternative to pure platinum. The bimetallics consisting of Pt and a metal M (denoted here as Pt–M, with M usually a first-row transition metal such as Cr, Fe, Co, and Ni) exhibit 2 to 10 times the catalytic activity for the oxygen reduction reaction (ORR) compared to pure Pt.[1-4] However, the extent of enhancement has varied widely among different investigators even for the same M, and the explanation as to why the bimetallic electrocatalysts perform better has also varied. Despite numerous studies, there is almost a complete lack of agreement regarding the fundamental enhancement processes occurring at the surface of these Pt–M bimetallic clusters.

Several studies on the kinetics or catalytic activity of Pt-based bimetallic clusters have been performed over the past 25 years in phosphoric acid fuel cells (PAFCs) and PEMFCs, and the results are usually indicated as a net gain factor in current density relative to pure Pt. An increase in mass activity (mA/mg at 0.90 V) by a factor of 1.5 to 2.5 was seen with Pt–Cr catalysts and for Pt–Co–Cr in PAFCs.[1-4] However, similar studies done by both Beard and Ross[5] and separately by Glass et al.[6] did not find much increase in mass activity with Pt–Co and Pt–Cr. Half-cell experiments by Min et al.[7] showed enhancement factors of 2 to 5 with Pt–Cr, Pt–Ni, and Pt–Co in PAFCs. Others, using a PEMFC and similar bimetallics, found similar enhancement factors of 2-3.[8,9] Toda et al.[10] reported the largest enhancement factors, as large as 10, for sputtered bimetallic films containing Pt with Ni, Co, or Fe relative to similarly prepared pure Pt films in 0.1 M $HClO_4$. Studies using Pt–Ni and Pt–Co bulk alloys in aqueous electrolyte found smaller enhancements on the order of 1.5-2;[11] however, similar experiments by Stamenkovic et al.[12] found a factor of 4 increase for Pt_3Ni. It is apparent that there is much variation in the enhancement factors obtained.

Comparing the above catalytic enhancement factors is difficult and complicated, because the kinetic measurements were made under different electrolytes (PAFCs, PEMFCs, and in $HClO_4$), with different catalyst geometries (Pt–M particles on carbon, sputtered thin bimetallic films on silica, and bulk alloys), and with different preparation procedures (cosputtering vs high-temperature annealing in inert gases); these factors are expected to play a role and enhance the catalysts in different ways. For example, the presence of directly or contact adsorbed anions (determined by the electrolyte) almost surely affects the enhancement factor because of their affect on OH or O chemisorption.[13] The relative stabilities of bulk alloys to M atom leaching will be very different than that for very small clusters. The method for preparing the bimetallics almost surely affects the final composition and structure of the electrode surface, which will also alter the enhancement. For example, the enhancement factor differs widely for a bulk Pt_3Ni electrode before (75% Pt surface atoms) and after annealing (100% Pt surface atoms: a Pt skin).[12]

In this context it is very important to draw a distinction between the prior literature on phosphoric acid fuel cells (PAFCs) and more recent reports on aqueous acid systems including the PEMFCs. While in PAFCs the electrode is in a largely anhydrous system, in the PEMFC the electrode is in a more fully hydrated environment. This important difference will certainly alter the effect of water activation and formation of Pt oxides and the extent of anion coverage (phosphate anion), both potentially serving as a poison of Pt surface sites for oxygen reduction.

It has also been reported that the rate of the ORR is dependent on the shape and size of the particles.[14-19] For example, the specific activity (mA/cm^2 Pt) generally increases with particle size in most fuel cells up to a particle size of ~35 Å. However, such size effects must be separated from alloying effects. The Pt–M catalysts are generally prepared by the formation of carbon-supported Pt, followed by the deposition of the second metal on Pt/C, and then annealing or alloying at high temperatures in an inert atmosphere. This alloying process generally results in larger Pt–M particles compared to the original Pt particles. It is difficult, if not even meaningless, to compare relative kinetic reactivities without an in situ particle size measurement to correlate with the enhancement, because a significant part of the enhancement might just come from the different particle sizes. Although in many instances the particle size has been determined from H adsorption measurement, allowing specific activities to be determined, it is not clear that the extent of H adsorption is unaffected by the alloying, so the indicated particle sizes may not be correct.

It seems clear that alloying does enhance the activity of the electrocatalyst; however, the degree of enhancement has shown inconsistent results and the mechanisms proposed to account for such

* Electrochemical Society Active Member.
[c] Present address: Chemistry Division, Naval Research Laboratory, Washington, DC 20375-5342.
[d] Present address: Department of Chemical Engineering, Case Western Reserve University, Cleveland, OH 44106.
[z] E-mail: ramaker@gwu.edu

enhancement are as varied as the results themselves. Early proposed mechanisms for the enhancement emphasized the Pt–Pt bond distance.[9] Alloying with M changes the Pt–Pt bond distance in the cluster, and the extent of this change depends on the atomic radius and electronegativity of M as well as the M:Pt ratio. This mechanism suggests that an optimum Pt–Pt bond distance exists for two-site O_2 absorption; therefore, "volcano" plots,[9] similar to those found in the heterogeneous gas-phase catalysis literature, have been constructed and show a maximum in the activity vs the Pt–Pt bond distance. However, other data show that the maximum activity falls at different Pt–Pt distance depending on the alloying M, arguing at least that some other mechanism may be playing a role.[20] Other proposed mechanisms include surface roughness effects or reduced OH poisoning of Pt sites, the latter occurring either because of adsorbate lateral interactions or electronic effects.[5,9,11] Recent density functional theory (DFT) results point strongly to an electronic effect, the effect being the shifting of the d-band center increasingly away from the Fermi level in the bimetallics with highest reactivity.[21,22] However, it is not even clear whether alloying increases the rate of the rate-determining step (rds) in the ORR, or just increases the effective number of surface sites on which the ORR can occur. For example, the strong electronic effects evident in the DFT results mentioned above suggest strongly that the rds in the ORR would increase, but recent measurement and comparison of the activation energies for Pt_3Ni and Pt showed very little difference.[12] Reviews of the effects of alloying on the ORR have been published by Adzic[23] and Mukerjee.[24]

OH formation.— This work will examine the effect of alloying on OH adsorption on the Pt-M surface. It is well known that the kinetics of the ORR is dependent on the intermediate products produced, either OH^- or O_2H^-, which may be adsorbed on the Pt surface.[8,25,26] It is believed that alloying may reduce the formation of "poisons" or OH formation on the Pt surface sites, which frees up the Pt sites to participate in O_2 reduction.[12,27] Cyclic voltammetry results have been reported for Pt–M bimetallics, showing indirect evidence for a reduced affinity for O[H];[9,12,28-30] however, no direct spectroscopic evidence has been reported showing a reduced coverage by O[H] (O[H] here indicates OH or O) in the bimetallics.

The formation of adsorbed OH on Pt in water has been extensively studied. It is widely accepted that the oxidation of Pt surfaces in water occurs in distinct steps with the first step, the formation of an adsorbed OH species above 0.80 V vs a reversible hydrogen electrode (RHE). The mechanism proposed nearly 40 years ago by Bockris et al.[31] proceeds according to the following steps

$$Pt + H_2O \rightarrow PtOH + H^+ + e^- \quad \text{OH formation} \quad 0.85\text{–}1.10\ \text{V} \qquad [1]$$

$$Pt - OH \rightarrow PtO + H^+ + e^- \quad \text{Place exchange} \quad 1.10\text{–}1.40\ \text{V} \qquad [2]$$

$$PtO + H_2O \rightarrow PtO_2 + 2H^+ + 2e^- \quad \text{Pt oxide formation} \quad > 1.40\ \text{V} \qquad [3]$$

It is unclear why the bimetallics reduce O[H] formation. Studies have provided indirect evidence that Pt–OH formation in fuel cells results from the interaction of water with Pt as described above and not from the reaction of O_2.[30,32,33] Several theoretical calculations have shown that OH coadsorbs with water, stabilizing the OH through hydrogen bonding with the water.[34-36] Experimental results using low-energy electron diffraction (LEED) and reflection/absorption infrared spectroscopy (RAIRS) confirmed that on a Pt(111) surface, adsorbed O reacts with water to form an OH/H_2O mixture which is stabilized by H bonding.[37] However, the exact role of water in such adsorption in a fuel cell is unknown, because every effort is made to keep the electrode hydrated but not flooded by using highly concentrated acid electrolyte or even an exchange membrane. Many have suggested that the inhibition of OH on bimetallic surfaces arises from changes in the electronic structure of the cluster as a result of alloying or even changes in the physical structure of the cluster, such as the formation of a Pt skin.[14] Others have suggested that the M metal is indeed at the surface, and that the repulsion between OH species on the M and on the Pt sites decreases the coverage of O[H] on the Pt.[11] These widely different mechanisms clearly indicate that the effect of the alloying on the OH adsorption, the nature of the Pt–OH bonding, as well as the effect of the distribution or composition of the bimetallic, is still not well understood.

Surface segregation and leaching.— Knowledge of the surface morphology and composition of Pt–M clusters is crucial to understanding the adsorbate interactions on the bimetallic surfaces. There have been several studies reported over the years using a variety of techniques to characterize the Pt–M surface. These include extended X-ray absorption fine structure (EXAFS), X-ray photoelectron spectroscopy (XPS), Auger electron spectroscopy (AES), IR spectroscopy and various electrochemical techniques.[38-41] Using cyclic voltammetry, Schmidt et al.[42] integrated base voltammograms and made an estimate of the fraction of active Pt surface atoms. A 1:1 Pt–Ni catalyst showed 70% Pt atoms at the surface compared to only 58% Pt atoms in a 1:1 Pt–Co bimetallic. This indicated that the Pt–Ni particle surface was closer to that of pure Pt than in the Pt–Co case. The more Pt-like behavior for the Pt–Ni catalyst suggested that the Ni may have "leached" out from the surface. In another study, XPS results on some Pt–Fe, Pt–Ni, and Pt–Co thin-film electrodes showed an almost total absence of M atoms at the surface, which was also attributed to a leaching-out process of the M atoms, occurring either as a result of an acid wash used during the electrode preparation or exposing the electrode to potentials greater than 1.10 V RHE.[10] These results are consistent with studies by Mizukami et al. on similar bimetallic clusters.[43] Urian et al.[44] recently prepared two sets of Pt–M/C catalysts, acid washed in 1 M $HClO_4$ for 48 h at room temperature, and unwashed. The acid wash apparently removes the M metal from the surface, and XANES data supported this. After 9 h with the electrodes polarized at 0.90 V, the two electrodes (washed and unwashed) showed similar XANES results, suggesting leaching of the reactive M also occurs under polarization. However, both Stamenkovic et al.[11] and Paulus et al.[45] found that the Co in a Pt–Co sample did not leach out, and the cluster remained homogeneous. Studies done by Obradovic[46] and Bardi[47] on Pt–Co clusters showed similar results. This nonleaching character in Pt–Co was attributed to an electronic stabilization of the cobalt in the bimetallic. In still other work, low-energy electron diffraction (LEED) studies showed that in Pt–Co and Pt–Ni with a Pt_xM_{x-1} composition resulted in M-rich cluster surfaces.[48] In contrast, Stamenkovic et al.[12] found that, for Pt_3Ni, the as prepared sputtered surface contained 75% Pt atoms, and after annealing at 950 K contained 100% Pt (a Pt skin). These electrodes showed different reactivities in rotating disk studies, suggesting that the Ni at the surface did not leach out.

Unfortunately, the method of preparation and electrochemical treatment is different in many of these cases, so one cannot yet conclude anything fundamental about when M surface segregation or leaching will occur. Although DFT calculations by Norskov's group[49] do suggest a strong antisegregation effect in the case of Pt–Co and Pt–Fe, where the Fe and Co atoms prefer to remain in the interior of the cluster allowing for a Pt skin, the effects of leaching in acid or at raised potentials in electrolytes are not entirely known. Nevertheless, this summary should make it clear that knowledge of the surface composition of the cluster is critical, and it must be determined in situ in order to understand the catalytic activity differences found.

Not only is a determination of the surface composition of a cluster important, along with a determination of the true particle size, the extent of initial alloy formation must also be determined. A review by Antolini[50] examined the Pt–Pt bond distance or lattice constant for several Pt–M clusters determined previously using ei-

ther X-ray diffraction (XRD) or EXAFS. The lattice constant is a measure of alloy formation, because it is found that in true bulk alloys the Pt–Pt distance decreases with the amount of M as well as in direct relation to its electronegativity. Antolini's analysis reveals that the extent of alloy formation depends critically on the preparation procedure, such as the temperature or acid solution utilized in the preparation, as well as the choice of the alloying element. Using the lattice constant, the fraction of M alloyed could be determined, and a plot of the logarithm of this fraction vs $1/T$ enabled the activation energy to be obtained for that particular alloy formation. Not surprisingly, this energy of activation varied nearly linearly with the atomic radius of M, suggesting that bigger M atoms have a more difficult time diffusing into or mixing with the Pt. Further, the particle diameter was also determined, and from a similar plot of ln(diameter) vs $1/T$ an activation energy for particle growth was obtained. This activation energy depended strongly on the acidity of the support, and was relatively independent of M. It is clear from Antolini's review that the bimetallics considered show a variety of compositions (different from the starting mixture), morphologies, and particle sizes. Further, most were not "true alloys" in the sense that they did not have a homogeneous composition even after initial preparation. In summary, the preparation procedure for bimetallic clusters strongly affects the particle composition, morphology, and size, and this obviously affects the composition of the particle surface. It is obvious these factors must be taken into consideration when comparing the catalytic activity of certain bimetallic materials. To date this has not always been the case.

X-ray absorption spectroscopy.— The primary reason for the lack of detailed information on OH inhibition or extent of OH coverage on an electrode in an electrochemical cell, as well as some information on particle size and composition, is the absence of a general in situ spectroscopic technique that can provide such information. Until recently, XAS analysis has been limited to providing geometric information on systems with short-range order, i.e., the normal EXAFS technique. However, recent advances in the interpretation of XAS [in both EXAFS and X-ray absorption near-edge structure (XANES)] now enable XANES to provide direct adsorbate binding site information along with the usual particle size and composition from EXAFS.[51] It has been reported recently that the electron scattering producing the Pt L_3 XANES is very sensitive to the adsorption of both O and H. Using a novel analysis technique that allows isolation of this Pt-adsorbate scattering, combined with theoretical calculations, allows for the in situ determination of adsorption sites (i.e., atop, bridged, threefold) on platinum electrodes utilizing Pt $L_{2,3}$ XANES.[52,53] These XANES data can be interpreted with full multiple scattering theoretical results from the FEFF 8.0 code[54] and local density functional (LDF) results using the Amsterdam Density Functional (ADF) code.[55] Comparison of theory with experimental data allows unique spectral signatures to be determined for H, OH, and O in atop, bridged, and threefold face-centered cubic (fcc) absorption sites respectively. Using this technique, Teliska et al.[52,53] have previously determined the adsorption sites and changes with coverage of atomic H, OH, and O on a Pt/C electrode in an aqueous $HClO_4$ or H_2SO_4 electrolyte.

In this paper we present Pt L_3 XAS studies on Pt-based bimetallic clusters to determine the cluster morphology, particle size, and the effects of alloying on the extent of OH formation in situ in an electrochemical cell at various potentials. This information then allows the catalytic activity of the bimetallic clusters to be related to the surface composition and OH coverage.

Experimental and Analysis Details

Since this investigation constitutes further work on the same series of samples considered previously,[9,28] the details of the preparation procedure and structure characterization will be given only briefly here. In these prior studies, structure property relationships were determined using a combination of ex situ XRD (powder diffractometer) and in situ XAS and correlated with their activity for oxygen reduction in a PEMFC environment. The following section gives details of the XANES and EXAFS analysis procedures, which were conducted following this previously published work on the same electrocatalysts.

Table I. Structural characteristics of the Pt and Pt bimetallic electrocatalyst using powder XRD data at 1.54 Å and XANES data.

Electrocatalyst	Lattice parameter	Pt–Pt bond distance (Å)	Average particle size (Å)	Atomic ratio (Pt:M) (from in situ XANES)
Pt/C	3.927	2.777	31	
Pt–Mn/C	3.897	2.756	55	69/31
Pt–Cr/C	3.874	2.740	56	73/27
Pt–Fe/C	3.861	2.730	55	72/28
Pt–Co/C	3.852	2.724	59	74/26
Pt–Ni/C	3.822	2.703	56	71/29

Previously reported[9,28] XAS data from five carbon supported binary Pt bimetallic electrocatalysts (Pt–Cr, Pt–Mn, Pt–Fe, Pt–Co, and Pt–Ni), procured from E-TEK Inc. (a division of De Nora, North America, Somerset, NJ) and supported on high surface area carbon (Vulcan XC-72, Cabot Corp.) were considered. All electrocatalysts had a metal loading on carbon (Vulcan XC-72, Cabot Corp.) of 20 wt %, similar to that used in previous investigations of PEMFCs.[56,57] A pure Pt/C sample with the same metal loading on carbon was used as a control (also obtained from E-TEK Inc.). The preparation methodology used was the well-known colloidal "sol" and carbothermic reduction methods.[58-61] In these methods, an oxide of the second alloying element is incorporated into the supported Pt/C electrocatalyst. When this is subjected to carbothermic reduction under inert conditions at 900°C for 9 h, the crystallites undergo reduction and alloying on the carbon support, thus providing for supported bimetallic nanoparticles. The nominal atomic ratios in the bimetallics were 3:1 (Pt:M); these were verified using in situ XANES measurements as described previously[9] (see Table I).

Previously reported[9] XRD analysis of these electrocatalysts showed a very high degree of crystallinity for these samples. Fits of the XRD data to an indexing routine showed that all the patterns (Pt and Pt bimetallics) corresponded to a fcc lattice. The lattice parameters obtained are summarized in Table I. In addition, the Pt–Pt particle sizes (Table I) assuming a fcc lattice were calculated based on X-ray line broadening analysis using the Scherrer equation. Bimetallics of Pt with the first-row transition elements (Cr to Ni) result in a lowering of the lattice parameters; hence, the Pt–Pt bond distances confirm partial formation of an alloy. Further, there is a smooth, inverse relationship between the measured lattice parameters and the electronegativity of the alloying element. From a comparison of the XRD pattern with a standard JCPDS database, the Pt bimetallics were found to form an intermetallic crystalline structure with a primary Pt_3M–type superlattice phase having a fcc structure, and potential for a secondary Pt–M type lattice with a tetragonal structure. The extent of contribution from the secondary phase was estimated by the intensity of the diffraction lines due to the Pt–M phase [such as (001) and (220) diffraction lines in the Pt–M/C powder pattern]. Contribution from these secondary phases was found to be negligible. The particle size obtained using the Pt(111) diffraction line broadening showed that the bimetallic catalysts have a particle size somewhat larger than for Pt/C; however, there does not appear to be any trend with M in the particle size.

The in situ XAS measurements, carried out at the National Synchrotron Light Source (NSLS), Brookhaven National Laboratory (BNL) using beam line X-23 A-2, were conducted in transmission mode using an electrochemical cell and data acquisition setup described in detail elsewhere.[62] To ensure a uniform electrochemical environment for the catalyst, XAS measurements were done in 1 M $HClO_4$ with the electrodes in flooded mode. The XANES data were

recorded at both the Pt L_3 edge and at the alloying metal K edge for Pt–M bimetallics, and all of the data are reported relative to the RHE. The measurements were made at the open-circuit potential and at potentials of 0.00, 0.24, 0.54, 0.84, and 1.14 V vs RHE. Results of the detailed XANES analyses are reported here only for potentials at 0.84 and 1.14 V vs RHE.

The analysis of these data proceeded exactly similar to the techniques we have published previously.[52,53] To highlight the effects of adsorption on the surface, the experimental $\Delta\mu = \mu(\text{ads/Pt–M})\text{-}\mu(\text{Pt–M})$ for the Pt L_3 edge is obtained by subtracting the L_3 edges from one another, where the μ obtained at 0.54 V RHE in $HClO_4$ is used as the reference [i.e., μ(Pt–M)] in this work. At 0.54 V RHE, no H or O is expected on the surface, and in $HClO_4$ no directly absorbed ions are expected either (although some O[H] is known to exist on the Co at this potential; see below). The Co K-edge data were treated similarly to the Pt L_3-edge data by subtracting the Co K edges from one another, where the μ obtained at 0.54 V RHE in $HClO_4$ is also used as the reference.

As summarized previously, before taking the differences, $\Delta\mu$, the edges may have to be properly aligned in order to remove any initial-state core-level shifts or final-state screening effects due to the chemisorption of hydrogen or oxygen.[52,53] However, the clusters in this work are relatively large (3–6 nm) compared to those used in our earlier work (2–3 nm), and we have shown previously that such shifts are negligibly small due to the metallic character of the larger clusters.[53] Therefore, in this work the L_3 spectra for the Pt–M electrodes were subtracted directly without any shift in energy, but only after careful energy calibration. Energy calibration was performed using the Pt L_3 spectra for bulk Pt measured at the same time as that for the sample. Although no other energy shifts were allowed in this work, note that a very careful energy calibration of each spectrum with the bulk Pt is essential to obtain reliable $\Delta\mu$ difference spectra.

The EXAFS analysis was performed using the WINXAS code.[63] The pre-edge background was removed using a linear polynomial and the many-body S_o^2 factor fixed at 0.934, the value obtained using the FEFF8 code. The postedge background was removed using the normal spline techniques and smoothing criteria that leaves the atomic XAFS scattering in the χ function as described previously.[64-67] Reference phase and amplitude functions for the Pt–Pt scattering were obtained from FEFF8 calculations on the Pt_6 cluster discussed below. Because of the large interdependency between N and the Debye-Waller factor, σ^2, the latter was fixed at the values indicated in Table I. These values were determined from the average of the σ^2 obtained when allowing this parameter to vary among the four samples.

Theoretical calculations.— FEFF8 calculations were performed to interpret the $\Delta\mu$ spectra using a series of Pt_6O_x and $Pt_4M_2O_2$ clusters with geometric configuration shown in Fig. 3. In all of the calculations, unless otherwise noted, the theoretical $\Delta\mu$ is calculated as $\Delta\mu = \mu(\text{ads/Pt–M})\text{-}\mu(\text{Pt–M})$, where the μ(Pt–M) is obtained from the clean cluster $Pt_4M_2O_2$ with Pt–Pt bond distances of 2.67 Å and Pt–M distances of 2.55 Å. Throughout this work the indicated Pt_6 cluster (i.e., not alloyed) is utilized, with the Pt–Pt distance at 2.77 Å.

These rather small cluster sizes (much smaller than the actual size in typical electrochemical experiments) have been utilized previously[52,53] to model the H/Pt and O/Pt adsorption in an electrochemical cell, and have been shown to be adequate to model the $\Delta\mu$ signatures. These small clusters are adequate of course because the Pt–O scattering and change in Pt–Pt scattering is a very local phenomenon. The only contribution that may not be adequately modeled by these small clusters is the change in atomic XAFS contributions, but this term is quite small as discussed previously.[52,53] At potentials where the O moves below the Pt surface (i.e., formation of Pt oxide), the signature is known to change again,[53] but this signature change is not seen in this work as we remain below 1.15 V RHE, and as we will see below the formation of the oxide occurs only at higher potentials for the Pt–M bimetallics.

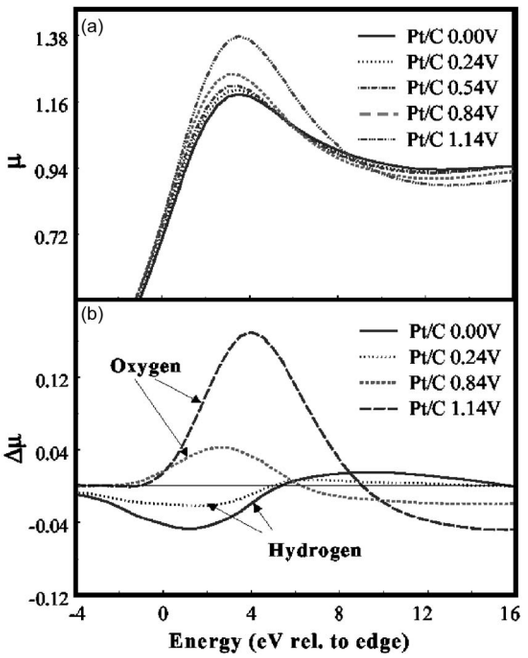

Figure 1. (a) Experimental L_3 absorption spectra, μ for the Pt/C electrode at the indicated potentials in 1 M $HClO_4$. These data were normalized at 50 eV using the smooth background function. (b) Experimental difference spectra $\Delta\mu = \mu(V) - \mu(0.54\ V)$ obtained from the data above, with typical O/Pt and H/Pt signatures indicated.

The FEFF8 code performs ab initio self-consistent field, real-space, full mutiple scattering calculations.[54] It is known that in the FEFF8 code, the results are quite dependent on the potentials used in the code. Previously, it was found that the Dirac-Hara potential with an imaginary part of 5 eV was optimal for describing the Pt–Pt and Pt–O scattering;[64,65] however, the emphasis in that optimization procedure was placed on the 25–150 eV region. Here, we are interested in the region below 40 eV. Although a more complete analysis in this energy region is required, the Hedin-Lundquist potential is preferred and used in this work to describe the Pt–O scattering following the work of Ankudinov et al.[54] and our previous work on Pt–H (Ref. 51 and 52) and Pt–O (Ref. 53) scattering.

The ATOMS code, developed by Ravel,[68] was used to generate a Pt cluster of approximately 200 atoms with the *Fm*3*m* space group, fcc, $a = 3.92$ of 8 shells. These clusters were used to model the Pt–Pt and Pt–M coordination numbers with different homogeneities for comparison with experiment. The average first-shell Pt–Pt and Pt–M coordination numbers were calculated for a pure Pt cluster, a true alloy with the metal atoms distributed evenly in a 3:1 Pt:M ratio, and with a "Pt skin." In the latter case the Pt skin consisted of two outer shells of Pt and the inner core in a Pt:M 2:1 ratio.

Results

Figure 1a shows the L_3 absorption spectra, μ, for a Pt/C electrode at several potentials. Similar data were obtained for the Pt–M bimetallics (M = Fe, Cr, Co, and Ni). Clear differences in μ, well above the noise level, are seen as a function of potential.

Figure 1b shows the experimental difference spectra, obtained from the data in Fig. 1a. Data for both the hydrogen (0.00 and 0.24 V) and oxygen (0.84 and 1.14 V) adsorption regions are shown. It is evident that the line shapes for hydrogen and oxygen are different and can be easily distinguished and assigned with theoretical references, and the amplitude reflects the relative amount of

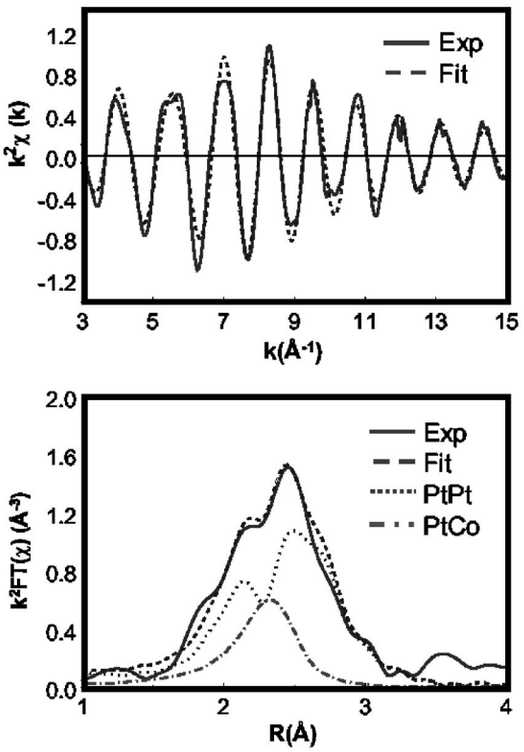

Figure 2. The experimental χ (top) and Fourier transform [FT(χ)] of $\chi(k^2, \Delta k = 1.5\ \text{Å}^{-1} < k < 17\ \text{Å}^{-1})$ (bottom) taken at 0.54 V (RHE) for the Pt–Co alloy. The fit (ΔR = 1.34–3 Å) for a two shell analysis (Pt–Pt and Pt–Co) is shown both in k (top) and R (bottom) space, along with the individual Pt–Pt + Pt–Co components (as indicated in the bottom) using theoretical references obtained from FEFF8 calculations on a Pt_4Co_2 cluster.

adsorbate in each case. Comparisons with theoretical FEFF8 calculations clearly verify that the signatures at 0.00 and 0.24 V primarily arise from H in the threefold fcc sites, and the data at 0.84 and 1.14 V from O in the threefold fcc sites as reported previously.[52,53]

Figure 2 shows experimental EXAFS data and theoretical fits in k- and R space for the Pt–Co metal cluster at 0.54 V. Also shown in R space are the Pt–Pt and Pt–M contributions, which are sufficiently different to allow for both coordination numbers and bond distances to be determined. Similar fits were obtained with the other bimetallics, and the results are given in Tables II-V.

Determination of OH coverage.— The theoretical $\Delta\mu$ fingerprints for O/Pt_6 from FEFF8 calculations are shown in Fig. 3 for a onefold atop and n-fold, bridged-O adsorption site; comparison with the experimental $\Delta\mu$ at 0.84 V is also included for comparison. These theoretical signatures have been verified by comparison with experimental data as reported previously.[53] The signature for atop adsorption is the most different from the rest, with that for the n-fold ($n > 1$) being indistinguishable from each other. Thus, it is possible to distinguish only atop from n-fold O[H] adsorption. As the coordination of O increases, the maximum in $\Delta\mu$ for atop O[H] around 2–3 eV moves to higher energy (to about 8 eV) with a negative-going feature appearing around 1 eV at the onset of subsurface O.[53] This change in $\Delta\mu$ with bonding site has been studied previously, and is attributed to a combination of changes in the Pt–Pt bond strength and charge transfer depending on the binding site.[53] In this work, the experimental $\Delta\mu$ will be used primarily to distinguish onefold atop adsorption from other n-fold O[H] adsorption, as suggested in Fig. 3.

Previously reported[69] local density functional calculations show that the O atom prefers to be at least doubly coordinated in n-fold coordinated positions, i.e., bridge or fcc sites, which completes the octet in the outer valence shell, consistent with simple chemical VSEPR (valence shell electron-pair repulsion) theory.[70] Similar calculations for the OH species on a Pt cluster show that the OH prefers to be onefold coordinated. We will therefore assume in this work that the atop species are OH and the n-fold species are O atoms.

Figure 4 shows experimental $\Delta\mu$ spectra for the Pt–M/C samples and the Pt/C at 0.84 V. The regions where the $\Delta\mu$ maxima in the theoretical signatures fall for onefold OH and n-fold O are indicated. At the onset of adsorption of oxygenated species, as water dissociates to form OH on the Pt surface around 0.80 V, a onefold coordinated OH species is indicated. Thus, we attribute the entire magnitude of $\Delta\mu$ over the range indicated to primarily OH adsorption. The decrease in magnitude of the spectral line shapes on these bimetallic materials confirms that alloying reduces atop OH adsorption when compared with pure Pt/C. The spectral magnitudes also indicate that there is a clear trend in the amount of OH adsorption at 0.84 V, decreasing as the alloying material is changed from Ni to Cr.

Table II. Summary of EXAFS first shell results for Pt/C. S_o^2 fixed at 0.934 as calculated by FEFF8 for all data in Tables II-VI. σ^2 is fixed at 0.006 for Pt–Pt and 0.007 for Pt–M; these values obtained from the average for all of the Pt–M samples.

V (RHE)	N [ΔN = 0.3[a]]	R (Å) [ΔR = 0.02[a]]	E_o (eV)
0.00	9.97	2.74	1.64
0.24	9.19	2.73	1.46
0.54	9.04	2.73	1.58
0.84	8.58	2.74	0.817
1.14	6.65	2.73	0.769
Ave.	8.78	2.73	

[a] Although the absolute values of ΔN and ΔR are certainly larger than that indicated, the variation in the values of N and R with potential are believed to be meaningful down to the values indicated in Tables II-VI.

Table III. Summary of EXAFS first shell results for Pt–Co. See Table II caption and footnote for details.

	Pt–Pt			Pt–Co		
V (RHE)	N [ΔN = 0.3]	R (Å) [ΔR = 0.02]	E_o (eV)	N [ΔN = 0.3]	R (Å) [ΔR = 0.02]	E_o (eV)
0.00	7.51	2.71	0.772	1.88	2.67	2.49
0.24	7.42	2.71	2.08	1.96	2.65	−1.42
0.54	7.16	2.71	1.10	1.90	2.66	2.06
0.84	7.01	2.70	0.362	2.28	2.67	2.44
1.14	7.26	2.71	0.431	1.84	2.67	2.24
Ave.	7.27	2.71		1.97	2.67	

Table IV. Summary of EXAFS first-shell results for Pt–Ni. See Table II caption and footnote.

	Pt–Pt			Pt–Ni		
V (RHE)	*N* [$\Delta N = 0.3$]	*R* (Å) [$\Delta R = 0.02$]	E_o (eV)	*N* [$\Delta N = 0.3$]	*R* (Å) [$\Delta R = 0.02$]	E_o (eV)
0.24	7.60	2.71	0.147	1.89	2.67	1.94
0.54	7.63	2.71	0.639	1.89	2.67	2.40
0.84	7.58	2.71	0.675	1.84	2.67	2.45
Ave.	7.67	2.71		1.89	2.67	2.40

Determination of cluster morphology.— In order to gain information regarding the cluster morphology and metal distribution, EXAFS analyses on the data were performed. The Pt–Pt and Pt–M coordination numbers and bond distances obtained from a two-shell EXAFS fit (one in the case of pure Pt) are presented in Tables II-VI. These results reveal that the particles have a total coordination number (Pt–Pt + Pt–M) around 9.0–10.5, and therefore have an average particle size of around 3.5–5 nm (containing about 200–800 atoms) based on model cluster calculations assuming spherical clusters.[71] Previous XRD analysis on these same ETEK catalysts (Table I) suggests particle sizes even larger, roughly 5–6 nm.[9,16,27] Further, these particles show a Pt–Pt bond distance generally smaller (2.71 Å) compared to that in bulk Pt (2.77 Å), consistent with Table I and that found previously even for pure small Pt clusters.[72-77] The coordination numbers for both Pt–Pt and Pt–M show no systematic variation with potential (except for pure Pt), indicating that significant Pt oxide formation has not set in up to 1.14 V, because after oxide formation the Pt–Pt coordination number is known to decrease rather sharply.[53] Perhaps the most interesting aspect of these results is a comparison of the Pt–M/Pt–Pt coordination number ratio, which varies from 0.27 to 0.47. This ratio is plotted in Fig. 5 vs the number of M 3d electrons, and strongly suggests that the homogeneity of these clusters is varying significantly depending on the metal M.

In order to gain an understanding of how the Pt–M/Pt–Pt ratio can vary depending on the particle homogeneity, spherical model clusters containing around 200 atoms were built up using the ATOMS code. The average coordination numbers were then calculated for a pure Pt cluster (with a Pt–Pt N of 9.9), a homogeneous cluster with a Pt:M ratio of 3:1, and for a cluster with a Pt skin about two layers thick and an inner core with a Pt:M ratio of roughly 2:1. For a homogeneous model cluster the Pt–M/Pt–Pt ratio is found to be around 0.25, which is expected with a 3:1 Pt–M ratio. The only way to increase this ratio is to move more M atoms to higher coordination, that is, into the interior of the cluster. The model cluster with two outer layers of Pt mimicking a Pt skin gives a Pt–M/Pt–Pt ratio of around 0.5. Figure 5 shows the experimental results and the theoretical results for the model clusters. It seems clear that there are primarily two different cluster morphologies among the four samples prepared in this work, the Pt–Fe and Pt–Cr clusters with a Pt skin of at least two Pt outer layers, and the Pt–Co and Pt–Ni clusters having a more homogeneous or true alloy composition with metal atoms at the surface.

Oxygen chemisorption.— Based on the in situ electrochemical and XAS data above, it is understood that OH binds in the atop position around 0.80–0.85 V. As the potential is increased and the O[H] coverage increases, O adsorbed in bridged and threefold fcc sites dominates.[53] Figure 6 shows experimental $\Delta\mu$ data for the Pt–Co and Pt–Cr samples at 1.14 V RHE. The Pt–Co data now clearly show two components, with the feature at low energy attributed to atop OH and the higher energy feature to *n*-fold bridged/fcc coordinated O. Thus, at higher potentials (adsorbate coverage), both chemisorbed OH and O can be seen spectroscopically in the same spectrum. The Pt–Cr shows primarily one peak at higher energy attributed to bridged/fcc bonded O. The intensity of the chemisorbed O is significantly lower for Pt–Co compared with Pt–Cr. We conclude that, although OH adsorption is strongly inhibited on the Pt–Cr cluster as indicated by Fig. 4 and has a Pt skin as indicated by Fig. 5, O adsorption is more strongly inhibited on the more homogeneous Pt–Co cluster.

Although not mentioned above, Fig. 4 shows one major feature in the range −4 to 6 eV for the Pt, Pt–Fe, and Pt–Cr samples, but two features for the Pt–Co and Pt–Ni cases. The first set of three samples contains only Pt on the surface, while the latter set of two has both Pt and M atoms on the surface. This suggests that the two peaks may come from two different environments surrounding the OH/Pt, namely near a M atom and away from a M atom on the surface. Perhaps the M atom near the Pt–OH transfers charge, changing the L_3 core level energy or even the valence energies. Two OH peaks are also visible in the $\Delta\mu$ spectra for Pt–Ru and Pt–Mo, when Ru or Mo islands (perhaps oxide islands) are known to exist on the Pt surface.[13] Thus, the double peaks in the $\Delta\mu$ OH spectra for Pt–Ni and Pt–Co, and their absence in Pt–Cr and Pt–Fe, provide further evidence for the different morphologies of these Pt bimetallics.

Co K-edge XAS.— Co K-edge XAS data were analyzed to determine the range of potentials where the Co is oxidized at the surface of the Pt–Co clusters. It is assumed, based on EXAFS analysis to be discussed below, that the Co atoms at the surface are oxidized above 0.54 V (covered with O[H]). Intuition would suggest this, because Co is much more reactive than Pt toward oxidation, and therefore the onset of Co oxidation should be much lower than the onset for OH/Pt around 0.80 V. Finally, theoretical results reported by Anderson et al.[78] suggest that the Co has OH on it all the way down to

Table V. Summary of EXAFS first-shell results for Pt–Cr. See Table II caption and footnote.

	Pt–Pt			Pt–Cr		
V (RHE)	*N* [$\Delta N = 0.3$]	*R* (Å) [$\Delta R = 0.02$]	E_o (eV)	*N* [$\Delta N = 0.3$]	*R* (Å) [$\Delta R = 0.02$]	E_o (eV)
0.00	7.97	2.71	1.87	2.82	2.68	−0.432
0.24	7.83	2.71	0.329	2.91	2.70	2.23
0.54	7.47	2.71	2.10	2.93	2.67	−0.452
0.84	7.54	2.71	1.17	2.72	2.67	−0.948
Ave.	7.70	2.71		2.84	2.68	

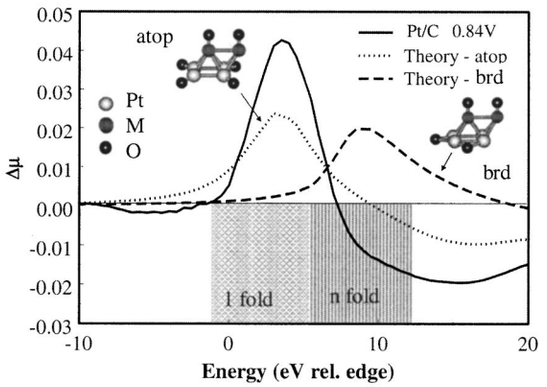

Figure 3. Experimental $\Delta\mu$ lineshape at 0.84 V RHE obtained from a Pt/C electrode. Also shown are theoretical signatures obtained from the FEFF8 code for a onefold atop adsorbed oxygen species, and in a bridged site, as shown by the $Pt_4M_2O_n$ model clusters with the positions of the Pt and M atoms (M = Cr, Fe, Co, or Ni) indicated.

0.00 V. Therefore, we performed XANES analysis at 0.54, 0.24, and 0.00 V to determine if in fact Co is covered with O[H] throughout this potential range, or where the onset of O[H] occurs.

The experimental $\Delta\mu = \mu(V) - \mu(0.54\ V)$ as obtained from Co K-edge XANES data at 0.24 and 0.00 V are plotted in Fig. 7. The overall intensities are quite small; therefore, the noise level is significant, particularly for the data at 0.24 V, but the data suggest that the $\Delta\mu$ signatures are somewhat similar at 0.00 and 0.24 V, and that this signature is much larger at 0.00 V. This strongly suggests that the O[H] coverage begins to decrease already at 0.24 V and decreases more sharply toward 0.00 V.

We attempt to confirm this decreasing OH coverage using FEFF8 calculations. To calculate the appropriate $\Delta\mu$ signature with FEFF8, O atoms are placed on Co atoms in the atop position at 2.0 Å above each Co atom, as shown in Fig. 7. This represents our model for the reference at 0.54 V. We replace the OH with H atoms at 2.0 Å above the Co, and also place H_2O molecules at 2.0 Å above the H atoms to represent water in the double layer. This represents our model of the Pt–Co electrode at 0.00 V. As can be seen in Fig. 7, the theoretical $\Delta\mu$ spectrum reasonably reproduces the two low-energy features in the experimental data, and also reproduces the higher energy oscillations. The theoretical $\Delta\mu$ was scaled to fit the experimental data and shifted by 5 eV (FEFF8 always requires some shift for best alignment with experiment). This reasonable agreement between the theoretical and experimental $\Delta\mu$ confirms that H replaces the OH on the Co, this process beginning (albeit it small) perhaps around 0.24 V.

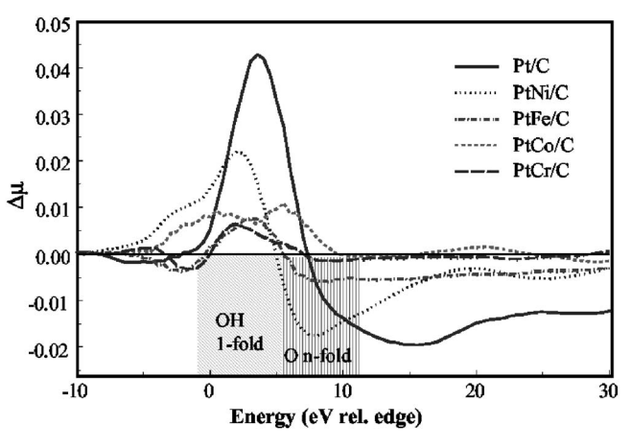

Figure 4. Experimental $\Delta\mu$ for Pt–M/C alloys and Pt/C at 0.84 V in 0.1 M $HClO_4$. The energy range where the theoretical onefold and *n*-fold $\Delta\mu$ maxima fall are indicated. The amount of atop OH on the alloys increases as the alloying metal is changed from Cr to Ni.

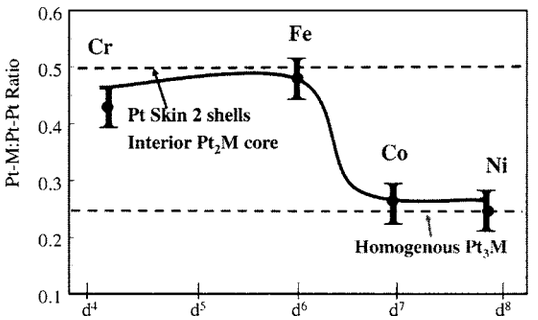

Figure 5. Results obtained (solid line) from EXAFS analysis of the Pt–M alloys and (horizontal dashed lines) from theoretical model clusters as described in the text.

Co K-edge data [i.e., Fourier transform (FT) of χ] also taken at 0.00, 0.24, and 0.54 V are shown in Fig. 8. Note the remarkable similarity between the data at 0.24 and 0.54 V, and the significant change in the Fourier transform occurring at 0.00 V. Thus, even without any EXAFS analysis, the data indicate something significant has changed with respect to the Co upon going from 0.24 to 0.00 V. A complete EXAFS analysis requires fitting five different shells to this data (Pt–Pt, Pt–Co, Pt–H, Pt–O_{short}, and Pt–O_{long}) over the range 1 Å $< R <$ 2.5 Å. This leads to significant linear dependencies and statistical inaccuracies; nevertheless, such an analysis is in progress and is not the focus of this work. Preliminary results suggest that dominant contributions to the various peaks are as those indicated in Fig. 8.

The FT at 0.00 V shows a loss of the Co–O[H] peak at 1.5 Å and a new intensity at 1.2 Å and at 1.8–2.0 Å which is not seen in the 0.24 and 0.54 V spectra. The 1.2 Å peak is attributed to the adsorption of H, and the additional intensity at 1.9 Å to water in the double-layer H bonded to the H atoms on the surface, as illustrated by the cluster in Fig. 7. This scattering from water in the double layer, which falls right at the principal Pt–Pt peak, is consistent with previous EXAFS data taken in an electrochemical cell.[79] Thus, these EXAFS results, although qualitative, are consistent with our interpretation of the XANES data and prior theoretical results[78] showing that the Co has chemisorbed O[H] on it all the way down to 0.24 V and beyond, but clearly at 0.00 V this O[H] is partially or totally replaced by H. Further, it confirms that the PtCo sample indeed does have Co on the surface rather than possessing a pure Pt skin.

Discussion

As mentioned in the beginning of this article, the importance of OH poisoning and its effects on a Pt electrode in a fuel cell has been controversial. Our XAS data clearly show OH species adsorbed in an atop site on Pt at 0.84 V vs RHE. It is clear from our results that alloying does significantly decreases the amount of OH adsorption in all cases. However, there is also a strong dependence on the metal M; the amount of OH on Pt–Ni and Pt–Co is much higher compared to that for Pt–Fe and Pt–Cr at 0.80 V. At 1.10 V, however, more O is adsorbed in the bridge/fcc sites on the Pt–Cr compared to the Pt–Co. These results are summarized in Fig. 9.

The EXAFS results show that the morphology of the Pt–Ni and Pt–Co clusters as prepared in this work are very different than the Pt–Fe and Pt–Cr clusters, the former homogeneous, the latter with a Pt skin. This difference provides some information as to the dominant mechanism for OH inhibition with the bimetallics. Two mechanisms, proposed previously, are considered below: Electronic effects

Table VI. Summary of EXAFS first-shell results for Pt–Fe. See Table II caption and footnote.

	Pt–Pt			Pt–Fe		
V (RHE)	*N* [$\Delta N = 0.3$]	*R* (Å) [$\Delta R = 0.02$]	E_o (eV)	*N* [$\Delta N = 0.3$]	*R* (Å) [$\Delta R = 0.02$]	E_o (eV)
0.24	5.54	2.74	3.29	4.48	2.70	4.40
0.54	6.28	2.71	−3.13	4.01	2.72	4.76
0.84	5.31	2.74	−3.40	4.46	2.69	3.84
Ave.	5.71	2.73		4.32	2.70	

induced by the M metal in the bimetallic, and lateral interactions between OH on the M and on the Pt as illustrated in Fig. 10.

Electronic effects.— One of the previously proposed mechanisms for OH inhibition is an altered electronic change in the Pt as a result of alloying.[9,16] These electronic changes include changes in the d band orbital vacancies, or changes in the physical structure (bond distance and coordination numbers) relative to pure Pt as a result of alloying. It has been suggested previously that the alloying metal M may lie below the surface with a Pt skin.[27] If the surface of the catalyst is mainly Pt, this rules out the lateral interaction mechanism to be described below, but may result in a decreased affinity for the formation of Pt–OH via an electronic effect.[78] Such an electronic effect would be expected to shift the onset for adsorption of OH, and hence provide the most dramatic effect at low potential, e.g., 0.84 V, but not be as significant at higher potentials because the entire particle surface is still Pt. This is exactly what the XANES data show as summarized in Fig. 9, a dramatic decrease in OH coverage compared to pure Pt at 0.84 V on the Pt–Fe and Pt–Cr clusters, but a smaller decrease in O coverage at 1.14 V, at least compared to the decrease with Pt–Co and Pt–Ni.

Lateral interactions.— Another possible mechanism for OH inhibition, suggested by Paulus et al.,[11,45] is adsorbate-adsorbate lateral interactions which arise when surface segregation has not taken place and the cluster is more homogeneous with metal M atoms present at the surface. Since the more reactive M atoms at the surface exists as M–OH above 0.24 V (at least for Pt–Co as shown above), these OH groups can repel other O[H] groups that want to come down on the surface Pt atoms at or above 0.84 V. Figure 10 shows a pictorial view of the electronic and lateral interactions.

The EXAFS results indicate that the Co and Ni bimetallics as prepared in this work are more homogeneous alloys with M atoms at the surface. The effectiveness of the lateral interactions should increase with coverage, since the first atoms to adsorb on the Pt can "steer clear" of the M atoms, but at higher coverage these preferred sites become occupied, leaving only the sites near the M atoms where the lateral interactions are the largest. Thus, the O[H] inhibition on Pt–Co and Pt–Ni should be the most effective at higher coverage, as verified by the XANES data in Fig. 6 taken at 1.14 V. At 1.14 V the O coverage is much lower on Pt–Co compared to Pt–Cr.

Correlation of XANES results with fuel cell data and CV plots.— We suggest above that the electronic mechanism is more effective at inhibiting OH adsorption around 0.70–0.90 V, while the lateral interaction mechanism is more effective at inhibiting O[H] at higher coverage and hence higher potential (0.90–1.20 V). Figure 10 shows the current, I_{900}, at 900 mV vs RHE reported previously by Mukerjee et al.[9,27] on these same samples vs the $\Delta\mu$ amplitude reflecting the OH coverage at 0.80 V. The relative OH coverage at 0.80 V is indicated by $\text{area}_{\Delta\mu}$, determined by integrating the $\Delta\mu$ curves in Fig. 4 from −5 to 10 eV (i.e., obtaining the area under the curve). Mukerjee et al.[9] normalized the I_{900} currents relative to the electroactive surface area as determined by integrating the faradaic *H* current from 0.10 to 0.30 V to account for particle size and for surface Pt composition (i.e., possible M atoms at the surface). Thus, the reported currents, I_{900} (mA/cm^2 Pt), and $\text{area}_{\Delta\mu}$ plotted in Fig. 10 have taken into account all of the effects of particle size and surface composition.

A clear linear correlation is found in Fig. 10 showing the direct effect of the OH poisoning, and this alone can account for the activity enhancement seen in Pt-based bimetallic catalysts in a fuel cell. Thus, no significant change in the initial rds involving the O_2 adsorption is needed to explain the enhancement. The plot suggests that "full" OH coverage is obtained when $\text{area}_{\Delta\mu}$ equals 5.5 at I_{900}

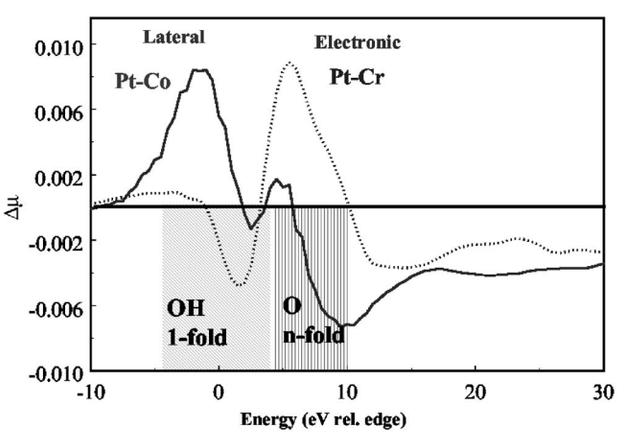

Figure 6. Oxygen adsorption at higher coverage (1.14 V) for the Pt–Co and Pr–Cr alloys. The energy regions where the FEFF8 theoretical $\Delta\mu$ maxima for onefold atop and *n*-fold O occur are indicated.

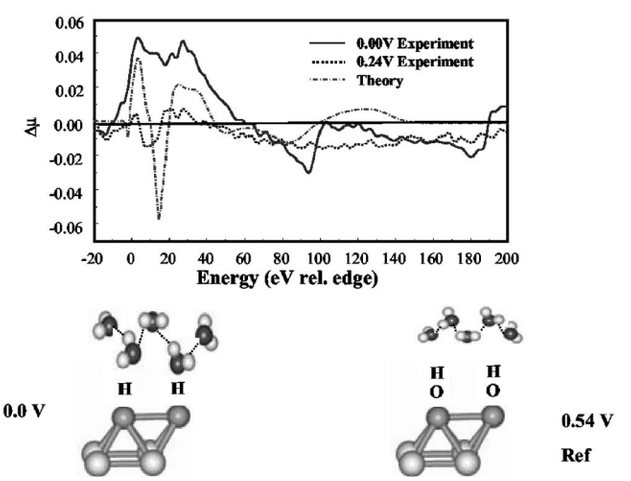

Figure 7. Co K-edge XANES difference spectrum, $\Delta\mu = \mu(V) - \mu(0.54\ V)$, at 0.00 and 0.24 V vs RHE. A FEFF8 theoretical calculation utilizing the clusters illustrated models H replacing OH on the Co atoms at 0.00 V as discussed in the text.

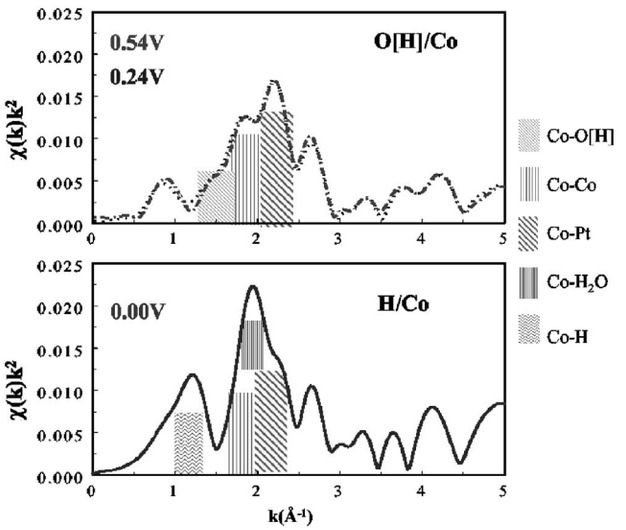

Figure 8. Co K-edge EXAFS data taken at the indicated potentials. The primary contributions to each feature in the Fourier transform are also indicated.

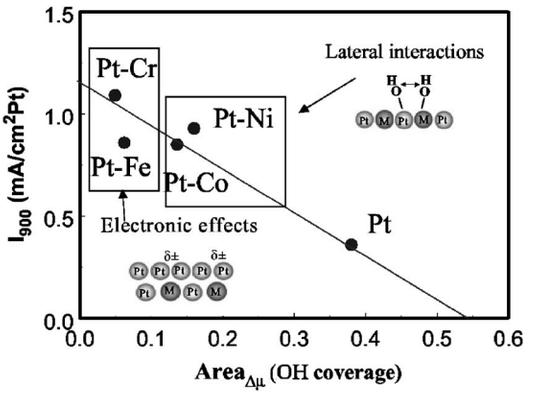

Figure 10. Plot of area$_{\Delta\mu}$ amplitude reflecting OH adsorption vs the normalized fuel cell current I_{900} (mA/cm^2 Pt) at 0.90 V (Ref. 46) obtained as described in the text. Insets illustrate the lateral interactions and the electronic effects, and the two samples in each case where these dominate.

equal to zero. It must be recognized, however, that the area$_{\Delta\mu}$ values here were obtained in an electrochemical cell containing 1 M $HClO_4$, not in an actual fuel cell, and thus the magnitudes of area$_{\Delta\mu}$ do not necessarily reflect the OH coverage in the fuel cells. Nevertheless, the estimated value of area$_{\Delta\mu}$ = 5.5 at full coverage is perfectly reasonable, because the theoretical atop signature in Fig. 3 was obtained from FEFF8 assuming a Pt–OH coordination of 1, and its area$_{\Delta\mu}$ in Fig. 3 is just slightly larger than that for Pt/C at 0.84 V. Thus, the OH coverage found at 0.84 V in the electrochemical cell appears to nicely model that in the PEM fuel cell at 0.90 V. Figure 10 also suggests that I_{900} could be as high as 3.3 times that for pure Pt (1.3 at zero OH coverage/0.36 for pure Pt) assuming zero OH poisoning. Finally, Fig. 10 shows that the primary difference between these four bimetallic samples appears to be the morphology, because PtCr and PtFe cluster together when the electronic effects dominate; PtCo and PtNi come together when the lateral interactions dominate. The electronic mechanism appears to be more effective for decreasing OH as expected in the fuel cell.

Figure 11 compares the positive-going scan of the cyclic voltammograms for Pt, and two of the bimetallics; namely for PtCo (homogeneous when lateral interaction dominate), and PtCr (Pt skin when the electronic effect dominates) in 1 M TFMSA. These cyclic voltammogram (CV) curves show an upward shift in potential for a given current in the order Pt < Pt–Co < Pt–Cr, in approximately the same order as the increase in fuel cell reactivity as indicated in Fig. 10. The current well above 0.90 V does not appear to reflect the effects of the lateral interactions in the Pt–Co, which should reduce the O coverage in this range as found from the XANES data. We suspect that the dominant components of the currents in Fig. 11 are reflecting OH adsorption, not O adsorption. This is a major benefit of the XANES analysis; it can distinguish between OH and O on the surface.

The H region from 0.00–0.30 V in Fig. 11 appears to reflect the morphology as found from the EXAFS data in this work as well as the effects of cluster size. These CV curves are similar in the H region to those reported by Mukerjee and Srinivasan[27] on the same samples in PEM fuel cells. The Pt–Co bimetallic shows a sharp peak around 0.10 V, right where the oxidation of the surface Co from CoH to CoOH occurs as discussed above. The oxidation of the H on the Pt at the surface of Pt–Co is also seen. In contrast, Pt–Cr, which EXAFS analysis indicates has a Pt skin, shows only the oxidation of the adsorbed H, although its intensity is reduced compared to the Pt/C because of the significantly larger cluster size for Pt–Cr.

The cyclic voltammograms, interpreted in the new light of the

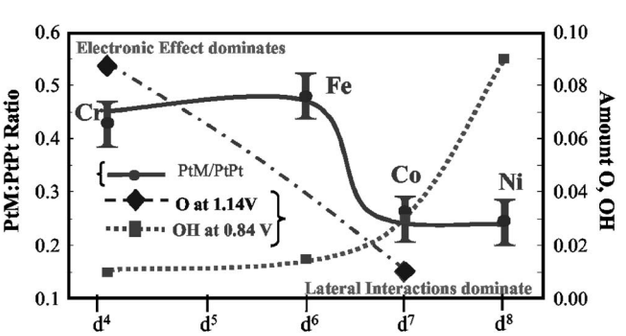

Figure 9. Summary of Δμ amplitudes at 0.84 V (representing atop OH) and the "O peak" in the Δμ spectrum taken at 1.14 V (right axis). Also indicated are the N_{Pt-M}:N_{Pt-Pt} ratios from Fig. 7 using the left axis.

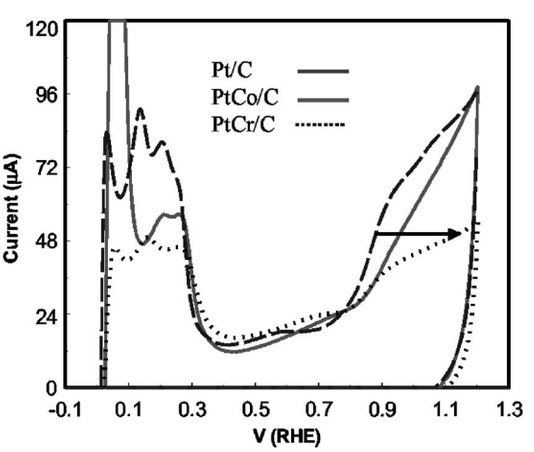

Figure 11. Cyclic voltammograms (scan rate of 50 mV/s) for Pt/C and two Pt–M alloys (homogeneous PtCo and PtCr with a Pt skin) in 1 M TFMSA, where the Pt–M CV curves have been normalized to have the same nonfaradaic or capacitance currents as that for the Pt/C electrode. The horizontal arrow shows the shift to higher potentials to reach a given current.

detailed information gained from the EXAFS and XANES analysis in this work, appear to be generally consistent with the findings in this work.

Pt enrichment at the surface.— We can only conjecture here on how or why Pt enrichment at the surface might occur to form a Pt skin. Previous studies by Toda et al.[10] directly observed a Pt skin using XPS; others have suggested that a Pt skin exists (Mukerjee;[9,16,27] early papers in Paulus et al.[45]) based on EXAFS or H chemisorption. In general, these authors conclude that the Pt skin forms by leaching of the more reactive M metals. However, it is unclear whether this forms as a result of the preparation, which sometimes includes an acid wash step (as performed on these samples) when the M atoms may leach out, or if it occurs after electrochemical processing. The latter has been directly confirmed by the XPS results of Toda et al.,[10] which showed M atoms at the surface in the as-prepared condition, and the absence of M atoms in at least the first two to three atom layers below the surface after the electrochemical experiments. However, these latter samples were prepared by cosputtering, so the bimetallics as deposited were perhaps not in the most stable state. Our bimetallic clusters, prepared by high-temperature anneal, might behave very differently and have the Pt surface enrichment already in the as-prepared state.

M-atom leaching might be thought of as consistent with our finding above, because the Pt–Cr and Pt–Fe clusters had Pt skins (i.e., the reactive Cr and Fe atoms possibly leached out), while the Pt–Co and Pt–Ni clusters (Co and Ni less reactive) were more homogeneous. However, the Pt–M/Pt–Pt coordination ratios found from the EXAFS for Pt–Cr and Pt–Fe suggest otherwise. A totally homogeneous cluster should give a Pt–M/Pt–Pt coordination ratio of 0.33 in a Pt_3M alloy, as found for Pt–Co and Pt–Ni. The higher Pt–M/Pt–Pt ratio of 0.4–0.5, found in Pt–Cr and Pt–Fe, cannot arise from M leaching out, but only from M atoms moving into the interior of the cluster during the alloying anneal process.

The details of metal segregation in alloys are not completely understood.[80] Most early studies were performed on the Pt–Ni and Pt–Co bimetallics, and most agree that the segregation depends on the surface energy and the size of the alloying metal.[81] Some theoretical estimates and experimental measurements[82-84] of the surface energies suggest that surface segregation should not occur in Pt–Ni (75:25), consistent with our EXAFS results for Pt–Ni. However, recent results by Stamenkovic et al.[12] on Pt_3Ni clusters show 75% surface Pt atoms in the as-prepared state, and 100% surface Pt atoms after annealing at high temperature, revealing a high *T* segregation. LEED results, along with calculated surface concentration profiles done on Pt–Co (75:25), also show that the surface is slightly enriched in Pt on the (111) faces.[85] Recent DFT calculations of Norskov's group[49] indicate a positive segregation energy of 0.37 and 0.46 eV for Fe and Co, respectively, for isolated M atoms in a Pt host, and suggest that both Fe and Co atoms indeed prefer to remain in the interior of the particle at thermodynamic equilibrium. Thus, in general a Pt skin is expected and found after a high-temperature anneal for all the M atoms utilized in this work.

The question then arises, why do the PtCo and PtNi samples in this work show a more homogeneous distribution? Equilibrium distributions should be reached faster with the Ni and Co, because of the smaller M-atom size, so we rule out a nonequilibrium distribution for Co and Ni. Perhaps the smaller Co and Ni atoms do not allow M rich (i.e., Pt_nM with *n* smaller than 3) alloys to form because of the greater lattice strain compared with Fe and Cr. If a significant Pt skin is to form in these clusters according to our model calculations, the interior must be richer in M. Further, the segregation energy has been found to depend on many factors, including particle size, the M-atom radius, and even the acidity of the support,[50] as summarized in the beginning. It is clear that much more work must be carried out on the formation or lack of a Pt skin and the effects of annealing before one can generally predict when a Pt skin will or will not occur.

Conclusions

X-ray absorption studies of Pt/C and Pt–M/C bimetallics combined with theoretical calculations provide direct spectroscopic evidence for OH inhibition on the electro-catalyst surface in the Pt-M clusters. This OH inhibition, going in the direction Pt < Pt–Ni < Pt–Co < Pt–Fe < Pt–Cr, is directly correlated with the previously reported kinetic reactivities for a fuel cell with these bimetallic compositions. The EXAFS analysis shows that the bimetallics as prepared in this work have different morphologies; the Pt–Ni and Pt–Co clusters are more homogeneous with M atoms on the surface, while the Pt–Fe and Pt–Cr have a Pt skin. The alloy composition in these samples determines which inhibition mechanism dominates. The electronic mechanism apparently dominates in the presence of the Pt skin, which is the most effective at inhibiting OH at low coverage, while the lateral interaction plays a more significant role on the O[H] species coming down when the Pt must reside at sites close to the M–OH groups existing at the surface. The mechanism for the Pt skin formation and the regularity for its existence are not clear.

Acknowledgments

The authors (S.M., V.S.M.) express their deepest appreciation to the Army Research Office for financial support (via both a single investigator and a MURI grant). The authors would also like to express their appreciation to the Department of Energy, Materials Science Division for their support in building and maintaining the National Synchrotron Light Source in Brookhaven National Laboratory (BNL, Upton, NY). Earlier pioneering work by Dr. James McBreen (BNl, Dept. of Materials Science) is deeply appreciated. His early instigation and support made this effort possible.

References

1. F. J. Luczak and D. A. Landsman, U.S. Pat. 4,447,506 (1984).
2. F. J. Luczak and A. Douglas, U.S. Pat. 4,711,829 (1987).
3. F. J. Luczak and D. A. Landsman, U.S. Pat. 4,677,092 (1987).
4. M. T. Paffet, G. J. Beery, and S. Gottesfeld, *J. Electrochem. Soc.*, **143**, 58 (1987).
5. B. Beard and P. Ross, *J. Electrochem. Soc.*, **137**, 3368 (1990).
6. J. T. Glass, G. L. Cahen, G. E. Stoner, and E. J. Taylor, *J. Electrochem. Soc.*, **134**, 58 (1987).
7. M. Min, J. Cho, K. Cho, and H. Kim, *Electrochim. Acta*, **45**, 4211 (2000).
8. D. B. Sepa, M. V. Vojnovic, L. M. Vracar, and A. Damjanovic, *Electrochim. Acta*, **32**, 129 (1987).
9. S. Mukerjee, S. Srinivasan, M. Soraiga, and J. McBreen, *J. Phys. Chem.*, **99**, 4577 (1995).
10. T. Toda, H. Igarashi, H. Uchida, and M. Watanabe, *J. Electrochem. Soc.*, **146**, 3750 (1999).
11. V. Stamenkovic, T. J. Schmidt, U. A. Paulus, N. M. Markovic, and P. N. Ross, Abstract 1053, The Electrochemical Society and the International Society of Electrochemistry Meeting Abstracts, Vol. 2001–2,San Franscisco, CA, Sept 2–7, 2001.
12. V. Stamenkovic, T. J. Schmidt, P. N. Ross, and N. M. Markovic, *J. Electroanal. Chem.*, **554–555**, 191 (2003).
13. M. Teliska, V. Murthi, S. Mukerjee, and D. E. Ramaker, *J. Phys. Chem. B*, Submitted; F. Scott, S. Mukerjee, and D. E. Ramaker, Submitted.
14. N. M. Markovic, H. A. Gasteiger, and P. N. Ross, *J. Electrochem. Soc.*, **144**, 1591 (1997).
15. K. Kinoshita, *Electrochemical Oxygen Technology*, p. 542, Wiley, New York (1992).
16. S. Mukerjee, *J. Appl. Electrochem.*, **20**, 537 (1990).
17. K. Kinoshita, in *Modern Aspects of Electrochemistry*, 14th ed., J. O'M. Bockris, B. E. Conway, and R. E. White, Editors, p. 557, Wiley, New York (1982).
18. M. L. Sattler and P. N. Ross, *Ultramicroscopy*, **20**, 21 (1986).
19. M. Peuckert, T. Yoneda, R. Dalla Betta, and M. Boudart, *J. Electrochem. Soc.*, **133**, 944 (1986).
20. J. A. S. Bett, in *Structural Effects in Electrocatalysis and Oxygen Electrochemistry*, D. Scherson, D. Tryk, M. Daroux, and X. Xing, Editors, PV 92–11, p. 573, The Electrochemical Society Proceedings Series, Pennington, NJ (1992).
21. Y. Xu, A. V. Ruban, and M. Mavrikakis, *J. Am. Chem. Soc.*, **126**, 4717 (2004).
22. P. B. Balbuena, D. Altomare, N. Vadlamani, S. Bingi, L. A. Agapito, and J. M. Seminario, *J. Phys. Chem. A*, **108**, 6378 (2004).
23. R. R. Adzic, in *Electrocatalysis*, J. Lipkowski and P. N. Ross, Editors, p. 197, Wiley VCH, New York (1998).
24. S. Mukerjee, in *Catalysis and Electrocatalysis at Nanoparticle Surfaces*, A. Wieckowski, E. R. Savinova, and C. G. Vayenas, Editors, Wiley-VCH, New York (1998).
25. E. Yeager, *Electrochim. Acta*, **29**, 1527 (1984).
26. A. Damjanovic, M. Genshaw, and J. O'M. Bockris, *J. Electrochem. Soc.*, **114**, 466 (1967).
27. S. Mukerjee and S. Srinivasan, *J. Electroanal. Chem.*, **357**, 201 (1993).
28. S. Mukerjee, S. Srinivasan, and M. P. Soriaga, *J. Electrochem. Soc.*, **142**, 1409

(1995).
29. B. E. Conway and D. M. Novak, *J. Electrochem. Soc.*, **128**, 956 (1981).
30. P. N. Ross and N. M. Markovic, *J. Electrochem. Soc.*, **137**, 3368 (1990).
31. A. K. N. Reddy, M. A. Genshaw, and J. O'M. Bockris, *J. Chem. Phys.*, **48**, 671 (1968).
32. M. R. Tarasevich and V. S. Vilinskaya, *Elektrokhimiya*, **9**, 96 (1973).
33. F. A. Uribe, T. E. Springer, M. S. Wilson, T. A. Zawodzinski Jr., and S. Gottesfeld, in *Oxygen Electrochemistry*, R. Adzic, F. C. Anson, and K. Kinoshita, Editors, PV 95–26, p. 50, The Electrochemical Society Proceedings Series, Pennington, NJ (1996).
34. A. Michaelides and P. Hu, *J. Chem. Phys.*, **114**, 513 (2001).
35. A. Michaelides and P. Hu, *J. Am. Chem. Soc.*, **123**, 4235 (2001).
36. K. Karlberg, F. E. Olson, M. Persson, and G. Wahnstrom, *J. Chem. Phys.*, **1919**, 4685 (2001).
37. C. Clay, S. Haq, and A. Hodgson, *Phys. Rev. Lett.*, **92**, 46102 (2004).
38. R. D. Gonzalez, *Appl. Surf. Sci.*, **19**, 181 (1984).
39. J. H. Sinflet, *Acc. Chem. Res.*, **20**, 134 (1987).
40. A. K. Santara, G. N. Subbanna, and C. N. R. Rao, *Surf. Sci.*, **317**, 259 (1994).
41. T. Rades, C. Pak, M. Polisset-Thfoin, R. Ryoo, and J. Fraissard, *Catal. Lett.*, **29**, 91 (1994).
42. T. J. Schmidt, H. A. Gasteiger, G. D. Stab, P. M. Urban, D. M. Kolb, and R. J. Behm, *J. Electrochem. Soc.*, **145**, 2354 (1998).
43. T. Mizukami, T. Nakamera, and P. Stonehart, *J. Electrochem. Soc.*, **141**, 2659 (1994).
44. R. C. Urian, V. Srinivasamurthi, and S. Mukerjee, in *Proton Conducting Membrane Fuel Cells III*, M. Murthy, T. F. Fuller, J. W. Van Zee, and S. Gottesfeld, Editors, PV 2002–31, p. 54, The Electrochemical Society Proceedings, Pennington, NJ (2005).
45. U. A. Paulus, A. Wokaun, G. G. Scherer, T. J. Schmidt, V. Stamenkovic, V. Radmilovic, N. M. Markovic, and P. N. Ross, *J. Phys. Chem. B*, **106**, 4181 (2002).
46. M. D. Obradovic, B. N. Grgur, and L. M. Vracar, *J. Electroanal. Chem.*, **548**, 69 (2003).
47. U. Bardi, B. Beard, and P. N. Ross, *J. Catal.*, **124**, 22 (1990).
48. J. M. Bugnard, Y. Gauthier, and R. Baudoing-Savois, *Surf. Sci.*, **344**, 42 (1995).
49. A. V. Ruban, H. L. Skriver, and J. K. Norskov, *Phys. Rev. B*, **59**, 15990 (1999).
50. E. Antolini, *Mater. Chem. Phys.*, **78**, 563 (2003).
51. D. E. Ramaker and D. C. Koningsberger, *Phys. Rev. Lett.*, **89**, 139701 (2002).
52. M. Teliska, W. E. O'Grady, and D. E. Ramaker, *J. Phys. Chem.*, **108**, 2333 (2004).
53. M. Teliska, W. E. O'Grady, and D. E. Ramaker, *J. Phys. Chem. B*, **109**, 8076 (2004).
54. A. L. Ankudinov, B. Ravel, and J. J. Rehr, *Phys. Rev. B*, **58**, 7565 (1998).
55. Amsterdam Density Functional Package ADF 2000.02, Department of Theoretical Chemistry, Vrije Universiteit, Amsterdam. http://www.scm.com
56. E. A. Ticianelli, C. R. Derouin, A. Redondo, and S. Srinivasan, *J. Electrochem. Soc.*, **135**, 2209 (1988).
57. S. Srinivisan, E. A. Ticianelli, C. R. Derouin, and A. J. Redondo, *J. Power Sources*, **22**, 359 (1988).
58. V. M. Jalan and C. L. Bushnell, U.S. Pat. 4,137,379 (1979).
59. V. M. Jalan, in Eur. Pat. Appl. 55,079,107 (1985).
60. D. A. Landsman and F. J. Luczak, in Belg. Pat. 4,373,014 (1981).
61. P. Stonehart, M. Watanabe, N. Yamamoto, T. Nakamura, N. Hara, and K. Tsurumi, in Jpn. Kokai Tokkyo Koho, 5,225,391 (1992).
62. J. McBreen, W. E. O'Grady, K. I. Pandya, R. W. Hoffman, and D. E. Sawyers, *Langmuir*, **3**, 428 (1987).
63. WinXAS 97, copyright Thorsten Ressler 1992–1997.
64. D. E. Ramaker, B. L. Mojet, D. C. Koningsberger, and W. E. O'Grady, *J. Phys.: Condens. Matter*, **10**, 8753 (1998).
65. G. E. van Dorssen, D. C. Koningsberger, and D. E. Ramaker, *J. Phys.: Condens. Matter*, **14**, 13529 (2003).
66. D. E. Ramaker, B. L. Mojet, J. T. Miller, and D. C. Koningsberer, *Top. Catal.*, **10**, 157 (2000).
67. D. C. Koningsberger, B. L. Mojet, J. T. Miller, and D. E. Ramaker, *J. Synchrotron Radiat.*, **6**, 135 (1999).
68. B. Ravel, *J. Synchrotron Radiat.*, **8**, 314 (2001).
69. D. E. Ramaker, M. Teliska, Y. Zhang, A. Yu. Stakheev, and D. C. Koningsberger, *Phys. Chem. Chem. Phys.*, **5**, 4492 (2003).
70. For example, see D. A. McQuarrie and P. A. Rock, *General Chemistry*, p. 290, W.H. Freeman, New York (1987).
71. J. de Graaf, A. J. van Dillen, K. P. de Jong, and D. C. Koningsberger, *J. Catal.*, **203**, 307 (2001); J. de Graaf, Ph.D. Dissertation, Utrecht University, Ridderkerk (2001).
72. D. C. Koningsberger, J. de Graaf, B. L. Mojet, D. E. Ramaker, and J. T. Miller, *Appl. Catal., A*, **191**, 205 (2000).
73. B. L. Mojet, J. T. Miller, D. E. Ramaker, and D. C. Koningsberger, *J. Catal.*, **186**, 373 (1999).
74. D. E. Ramaker, B. L. Mojet, M. T. Garriga Oostenbrink, J. T. Miller, and D. C. Koningsberger, *Phys. Chem. Chem. Phys.*, **1**, 2293 (1999).
75. D. C. Koningsberger, M. K. Oudenhuijzen, J. H. Bitter, and D. E. Ramaker, *Top. Catal.*, **10**, 167 (2000).
76. B. L. Mojet, D. E. Ramaker, J. T. Miller, and D. C. Koningsberger, *Catal. Lett.*, **62**, 15 (1999).
77. A. K. Shukla, R. K. Raman, N. A. Choudhury, K. R. Priolkar, P. R. Sarode, S. Emura, and R. Kumashiro, *J. Electroanal. Chem.*, **563**, 181 (2004).
78. A. B. Anderson, E. Grantscharova, and S. Seong, *J. Electrochem. Soc.*, **143**, 2075 (1996).
79. W. E. O'Grady, Private communication (2005).
80. M. Polak and L. Rubinovich, *Surf. Sci. Rep.*, **262**, 1 (1999).
81. C. Gallis, Thesis Universite Paris VI, France (1997).
82. G. Bozzolo, J. Ferrante, R. D. Noebe, B. Good, F. S. Honecy, and P. Abel, *Comput. Mater. Sci.*, **15**, 169 (1999).
83. Y. Gauthier, R. Baudoing, M. Lundberg, and J. Rundgren, *Phys. Rev. B*, **35**, 7867 (1987).
84. P. Weignard, B. Jelinek, W. Hofer, and P. Varga, *Surf. Sci.*, **301**, 306 (1994).
85. L. Z. Mezey and W. Hofer, *Surf. Sci.*, **352–354**, 15 (1996).